Journal Name

ARTICLE TYPE

Cite this: DOI: 00.0000/xxxxxxxxxx

Tuning conformational asymmetry in particle-forming diblock copolymer alloys†

Logan J. Case, Frank S. Bates, and Kevin D. Dorfman*

Received Date
Accepted Date

DOI: 00.0000/xxxxxxxxxx

Self-consistent field theory is employed to compute the phase behavior of binary blends of conformationally asymmetric, micelle-forming diblock copolymers with miscible corona blocks and immiscible core blocks (a diblock copolymer "alloy"). The calculations focus on establishing conditions that promote the formation of Laves phases by tuning the relative softness of the cores of the two different Laves phase particles via independent control of their conformational asymmetries. Increasing the conformational asymmetry of the more spherical particles of the Laves structure has a stabilizing effect, consistent with the expectations of increased imprinting of the Wigner-Seitz cells on the core/corona interface as conformational asymmetry increases. The resulting phase diagram in the temperature-blend composition space features a more stable Laves phase field than that predicted for conformationally symmetric systems. The phase field closes at low temperatures in favor of macrophase separation between a hexagonally-packed cylinder (hex) phase and a body-centered cubic phase. Companion calculations, using an alloy whose components do not produce a hex phase in the neat melt state, suggest that the Laves phase field in such a blend will persist at strong segregation.

1 Introduction

Compositionally asymmetric diblock polymer melts produce particulate phases when cooled below their order-disorder transition (ODT). For linear AB diblock copolymers, the ordered state selection is governed by three parameters: (i) the segregation strength χN, where χ is the Flory-Huggins parameter and N is the total degree of polymerization; (ii) the minority block volume fraction $f_A = N_A/N$, where N_A is the degree of polymerization of the minority block; and (iii) the conformational asymmetry $\varepsilon_{AB} = b_A/b_B$, where b_i is the statistical segment length of block i.[1–5] The classic theoretical diblock copolymer phase diagram focuses on systems with low conformational asymmetry ($\varepsilon_{AB} \approx 1$),[6–8] where the resulting micelles pack on a body-centered cubic (bcc) lattice,[9–11] with a narrow region of close-packing near the ODT.[7,12–14]

It is now recognized that increasing conformational asymmetry in compositionally asymmetric diblock copolymers gives rise to a different class of particle packings known as Frank-Kasper phases (Fig. 1a).[15–19] In contrast to bcc, which has a single particle type arranged on a high symmetry lattice, Frank-Kasper phases are low-symmetry, tetrahedrally close-packed phases possessing multiple particle types,[20,21] each with a distinct volume and, importantly, a distinct sphericity.[5,22,23] Conformational asymmetry furnishes two synergistic effects that ultimately combine to stabilize Frank-Kasper phases relative to bcc. First, larger ε_{AB} shifts the order-order transitions to larger f_A, delaying the onset of hexagonally packed cylinders (hex).[1,22,24–27] Second, larger ε_{AB} produces softer micellar cores that can be partially imprinted by the Voronoi cells of the lattice,[5,19,23,28–30] which introduces a tendency to prefer systems with a higher average sphericity of the constituent particles.[23] Taken together, these two effects lead to Frank-Kasper phases possessing a better balance of chain stretching against interfacial area than bcc as conformational asymmetry increases.[5,22,23] Among the 27 known Frank-Kasper phases in metallic alloys,[31] only σ[15,16,18,32–38] and A15[18,36] are believed to be equilibrium states in neat diblock copolymer melts. Non-equilibrium C14 or C15 Laves phases can be accessed via thermal processing,[17,35,39,40] but their emergence as equilibrium states is stymied by their large particle volume asymmetry (Fig. 1b).[37,41–44]

Since each particle type in a Frank-Kasper phase possesses a unique sphericity (Fig. 1c),[5,22,23] fully elucidating the role of conformational asymmetry on the formation of Frank-Kasper phases is challenging in a neat diblock copolymer melt because there is but a single conformational asymmetry parameter, ε_{AB}. To understand more deeply how conformational asymmetry impacts or-

Department of Chemical Engineering and Materials Science, University of Minnesota – Twin Cities, 421 Washington Ave SE, Minneapolis, Minnesota 55455, United States
Tel: +1 612 6245560; E-mail: dorfman@umn.edu

† Electronic Supplementary Information (ESI) available: Details of SCFT methodology; Common tangent and grand canonical ensemble results; impact of conformational asymmetry; list of candidate phases and their properties; Laves phase degeneracy data; details of phase diagram calculations. See DOI: 00.0000/00000000.

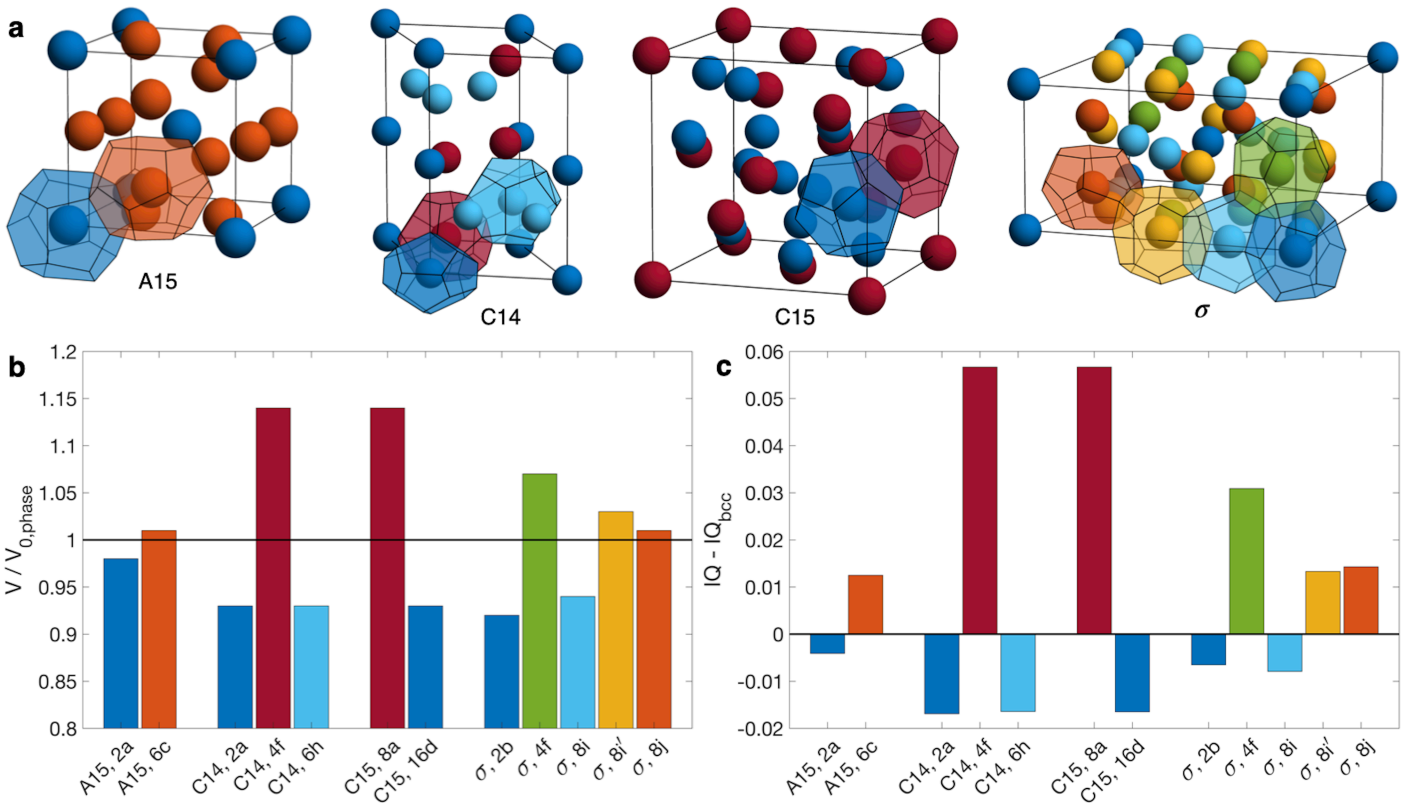

Fig. 1 (a) Illustration of the Frank-Kasper σ, A15, C14, and C15 phases, highlighting the symmetry-inequivalent particle positions and associated Wigner-Seitz cells. (b) Volume of each particle type relative to the number-averaged particle volume for the structure, $V_{0,\mathrm{phase}}$. (c) Isoperimetric quotient $\mathrm{IQ} = 36\pi \mathrm{V}^2/\mathrm{S}^3$ of each particle type as reported by Kim *et al.*,[17] relative to that of bcc, where V is the particle volume and S is the particle surface area. Bar colors in (b) and (c) match the colors of the corresponding particles in (a). Particles are labeled in (b) and (c) according to phase and Wyckoff position. Structures in (a) are generated using a Matlab program developed by Lindsay *et al.*[45]

dered state selection, it is desirable to control each particle type's conformational asymmetry independently. One approach to access such control is going beyond a neat AB diblock copolymer melt to a diblock copolymer alloy consisting of two (or more) diblock copolymers with miscible majority blocks and immiscible minority blocks.[46] The simplest such system is a binary alloy consisting of a blend of AB and B′C diblock copolymers,[46] where the prime notation indicates a different degree of polymerization. To achieve this objective, the χ-parameter between blocks A and C must be large enough to prevent mixing of the particle cores.[46] Such a binary blend possesses two conformational asymmetry parameters, $\varepsilon_{\mathrm{AB}}$ and $\varepsilon_{\mathrm{BC}}$, which quantify the softness of the AB and B′C micelle cores, respectively.

In the present contribution, we use self-consistent field theory (SCFT)[47,48] to investigate the ability of conformationally asymmetric block copolymer alloys to stabilize Laves phases. Laves phases are attractive for our purposes because they consist of two particles with disparate volumes and sphericities.[17,23,49] As a result, this system is ideally suited for studying the tunability of the different types of particle cores enabled by binary block copolymer alloys. Prior work has already demonstrated from SCFT the potential for diblock copolymer alloys to address the challenge imposed by the volume asymmetry of a Laves phase (Fig. 1b).[46] Here, we show that Laves phases can be further stabilized via differing conformational asymmetries in a polymer alloy, thereby providing a design strategy to address both volume asymmetry and sphericity asymmetry of the constituent particles, and clearly illustrating the power of controlling conformational asymmetry of each particle independently to enable the formation of complex particle packings in diblock copolymers.

2 Methods

Following prior work,[46] we select highly compositionally asymmetric diblocks with equal core block fraction $f_{\mathrm{A}} = f_{\mathrm{C}} = 0.20$ to promote formation of quasi-spherical micelles at sufficiently high segregation strength. To simplify the ensuing analysis, we choose symmetric segregation strengths for the individual diblock copolymers, such that $\chi_{\mathrm{AB}}N_{\mathrm{AB}} = \chi_{\mathrm{BC}}N_{\mathrm{B'C}} = \chi N$ where χ_{ij} is the Flory-Huggins interaction parameter between monomers i and j and N_{AB} and $N_{\mathrm{B'C}}$ are the degrees of polymerization of the AB and B′C chains, respectively. To enhance the immiscibility of A and C relative to A/B or B/C interactions, we select a larger Flory-Huggins parameter between monomers A and C such that $\chi_{\mathrm{AC}}N_{\mathrm{AB}} = 2(\chi N)$. In reporting our results, it is convenient to express the results in terms of temperature as well. To do so, we will assume that χ is purely enthalpic and set the reference temperature T_0 to correspond to $\chi N = 30$.

It is worthwhile to make a preliminary estimate here of where we might anticipate Laves phases to emerge in a conformationally asymmetric binary alloy, building on the prior analysis for confor-

mationally symmetric systems.[46] Stabilization of a Laves phase in this alloy system requires that (i) the AB and B′C form micelles with appropriate volume asymmetry $\alpha = V_{B'C}/V_{AB}$ and (ii) the chains are blended at a ratio which yields a particle stoichiometry of approximately 2:1.[46] If we choose the B′C diblock to form the larger micelles (the red particles in Fig. 1), the expected blend fraction for Laves phase formation is

$$\phi_{AB} = 1 - \phi_{B'C} = \frac{2}{2+\alpha} \tag{1}$$

as in prior work.[46] The preferred micelle radius for the AB diblock scales as its radius of gyration $R_{g,AB}$, and similarly for the B′C diblock, so the volume asymmetry can be written as $\alpha = (R^3_{g,B'C}/R^3_{g,AB})$. Using the unperturbed radius of gyration as a starting point for the particle size and Gaussian statistics, then $R_{g,AB}$ is given by $R^2_{g,AB} = R^2_{g,A} + R^2_{g,B}$, and similarly for $R_{g,B'C}$. The corresponding Laves phase volume asymmetry for a given set of AB and B′C chains is then

$$\alpha = \left(\frac{N_{B'C}}{N_{AB}}\right)^{3/2} \left[\frac{1 + f_C\left(\varepsilon^2_{BC} - 1\right)}{1 + f_A\left(\varepsilon^2_{AB} - 1\right)}\right]^{3/2} \tag{2}$$

where we have grouped the terms to highlight the separate contributions of the chain lengths in the first term, and the statistical segment lengths in the second term. Note that when all monomers have the same statistical segment lengths (i.e., $\varepsilon_{AB} = \varepsilon_{BC} = 1.0$), Equation 2 reduces to the result obtained previously for conformationally symmetric alloys.[46]

Our numerical analysis uses SCFT[47,48] with a Gaussian chain model[47,50,51] to predict the behavior of the alloy system. All calculations are performed using the C++ version of the open-source PSCF code using either the canonical or grand canonical ensembles.[52–54] More details about the particular methodologies employed to analyze phase equilibria or compute phase boundaries are available in the Supporting Information.

3 Results

Our first objective is to understand how chain length and conformational asymmetry affect the stability of Laves phases, using the independent control over conformational asymmetry to adjust the softness of the AB and B′C micelle cores for different chain lengths. We thus consider systems with chain length asymmetries $0.5 \leq N_{B'C}/N_{AB} \leq 2.0$ for conformational asymmetries of 1.00, 1.25, and 1.50 applied to (i) the AB diblock, (ii) the B′C diblock, and (iii) both the AB and B′C diblocks simultaneously. For each of these conditions, we performed canonical SCFT simulations of the C14 and C15 Laves phases and compared their free energies per chain of size N_{AB} (denoted by F/nk_BT) against potential macrophase separation via the common tangent construction.[55] Among the three most common Laves phases (C14, C15, and C36),[49] we consider only C14 and C15 because they are generally expected to be stable compared to C36,[56] and are the only Laves phases observed in block polymer systems.[17,35,37,39–41,57] Candidate phases for construction of the common tangent tie lines were face-centered cubic spheres (fcc), body-centered cubic spheres (bcc), and hexagonally-packed cylinders (hex), each with both AB-rich and B′C-rich varieties. At each condition, the common tangent representing macrophase separation for comparison to the Laves phases was taken to be the lowest-energy tangent among tangents formed by each (AB-rich, B′C-rich) phase pairing. In general, bcc-bcc macrophase separation is the relevant candidate to compare with the Laves phase, with the exception of a few cases of fcc-bcc macrophase separation. The analysis was performed at two segregation strengths, $\chi N = 25$ and $\chi N = 28$, chosen based on the neat diblock phase diagrams[25] such that a neat diblock melt with block fraction $f_i = 0.2$ and conformational asymmetry of $\varepsilon_{ij} = 1.0$ or $\varepsilon_{ij} = 1.5$, respectively, would be near the center of the bcc window. Details of this analysis are available in the Supporting Information.

Figure 2 depicts the lowest energy of the C14 Laves phase relative to macrophase separation at each of the conditions described above at $\chi N = 28$. Note that the Laves phases are nearly degenerate in free energy (see Fig. S3) consistent with prior literature;[17,39,46,56,58] thus selection of C14 over C15 for the analysis is inconsequential. At this segregation strength, the macrophase separation reference is dominated by coexistence of AB-rich and B′C-rich bcc morphologies; the only exceptions occur when B′C-rich fcc overtakes B′C-rich bcc at the highest conformational asymmetry condition ($\varepsilon_{ij} = 1.5$) for very low $N_{B'C}/N_{AB}$, highlighted by the shaded regions in the figure.

The data in Fig. 2 demonstrate the distinct effects of each conformational asymmetry on both the stability of the Laves phases and the chain length asymmetry most favorable to their formation. Increasing the conformational asymmetry of the AB diblock (Fig. 2a) generally destabilizes Laves phases while shifting the minima of the F vs $N_{B'C}/N_{AB}$ toward higher chain length asymmetry. If instead ε_{BC} is increased (Fig. 2b), the opposite effect is observed with the Laves phases becoming more stable with increasing conformational asymmetry and the minima of F vs $N_{B'C}/N_{AB}$ shifting to lower $N_{B'C}/N_{AB}$. Simultaneously increasing both ε_{AB} and ε_{BC} (Fig. 2c) leads to competition between these two opposing trends, resulting in only minimal changes to F vs $N_{B'C}/N_{AB}$.

The stabilizing effect of ε_{BC} and the destabilizing effect of ε_{AB} both can be attributed to the softening of micelle cores and the resultant imprinting on the polyhedral Wigner-Seitz cell.[5,19,23,28–30] As conformational asymmetry increases, faceting of the micelle core creates more interfacial area, but the thermodynamic cost, relative to micelle volume, is lower for more spherical polyhedra.[5,22,23] In neat diblock systems, Frank-Kasper phases are proposed to form at higher conformational asymmetry because their particles are, on average, more spherical than in bcc.[17,23] Critically, however, this does not mean that all Wigner-Seitz polyhedra in a Frank-Kasper phase are more spherical than those in bcc,[17] as shown in Fig. 1c. Rather, the thermodynamic benefits of the polyhedra that are more spherical (the red Laves phase particles in Fig. 1) tend to outweigh the costs of those that are less spherical. In the Laves phases, the smaller micelles (AB) reside in domains that are less spherical than bcc, while the larger micelles (B′C) are in more spherical domains.[17] Therefore, when increasing ε_{AB}, there is a thermodynamic cost (relative to bcc formation) incurred by deforming the small micelle cores without

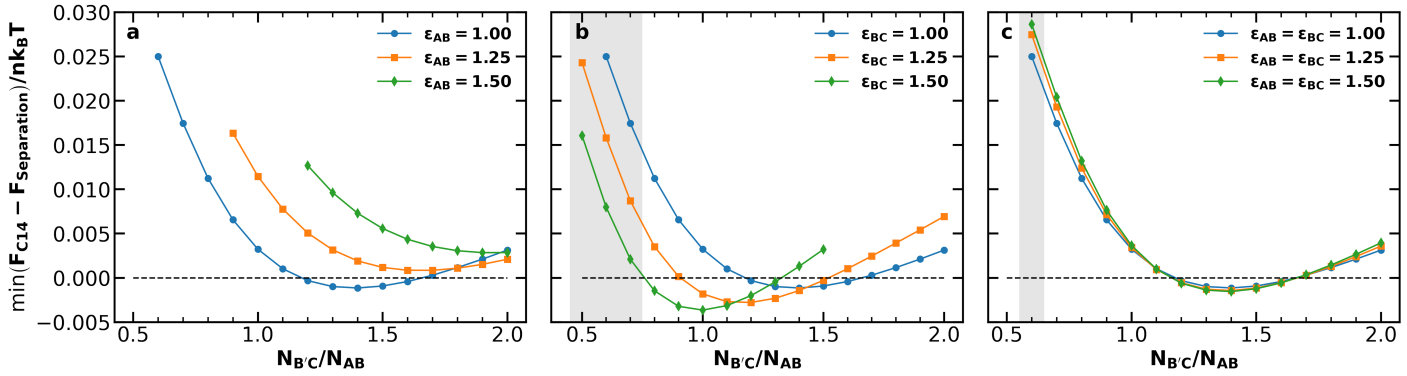

Fig. 2 Minimum free energy of the C14 Laves phase relative to the macrophase separation tangent line at various conformational asymmetries for (a) the AB diblock, (b) the B′C diblock, or (c) both the AB and B′C diblocks for $\chi_{AB}N_{AB} = \chi_{BC}N_{B'C} = 28.0$, $\chi_{AC}N_{AB} = 56.0$, and $f_A = f_C = 0.20$. Shaded regions indicate those in which B′C-rich fcc is used in the macrophase separation tangent, rather than B′C-rich bcc, which only correspond to $\varepsilon_{BC} = 1.5$ in (b) or $\varepsilon_{AB} = \varepsilon_{BC} = 1.5$ in (c). The same analysis performed at $\chi N = 25$ exhibits similar results (see Fig. S2).

the larger domains as a counter-balance; likewise, increasing ε_{BC} creates a relative thermodynamic benefit without the opposing cost of the smaller micelles.

The observed shifts in the locations of the F vs $N_{B'C}/N_{AB}$ minima result from the effects of conformational asymmetry on the radius of gyration of a diblock copolymer. Increasing ε_{ij} at fixed N increases the micelle volume. When increasing ε_{AB}, this swelling applies to the smaller particles in the Laves structure. Such changes reduce the volume asymmetry, making the Laves structure less stable. Increasing the chain length asymmetry compensates somewhat for the unfavorable swelling of AB micelles, resulting in the rightward shift of the curves. The reverse holds true for B′C: increasing ε_{BC} swells the larger particles for a given value of N, thus promoting excess volume asymmetry and demanding reduced length asymmetry in response to stabilize the Laves phase. In fact, the swelling induced by $\varepsilon_{BC} = 1.50$ is sufficient on its own to produce the requisite Laves volume asymmetry, with the observed minimum occurring at $N_{B'C}/N_{AB} = 1.0$.

Neither of these trends are evident in Fig. 2c, in which ε_{BC} and ε_{AB} are increased together. Instead, simultaneous changes to both conformational asymmetries obscure the competing effects described above, resulting in minimal changes to the free-energy curve. This condition is analogous to the single conformational asymmetry available in neat diblock melts obscuring the individual particle effects, and highlights the value of leveraging multiple conformational asymmetries. The same analysis as that in Fig. 2 was performed at $\chi N = 25$ and produced similar results (see Fig. S2). For both values of χN, the Laves phases had their lowest relative free energy when $\varepsilon_{BC} = 1.5$ and $N_{B'C}/N_{AB} = 1.0$, so this condition was selected for further analysis.

Having established the impacts of simultaneously varying conformational asymmetry and chain length, we now investigate the applicability of the simple estimate for the optimal conditions for Laves phase stability in Equation 2. Figure 3 compares the optimum $N_{B'C}/N_{AB}$ at $\chi N = 25$ and $\chi N = 28$ from our SCFT results against values predicted by Equation 2 with varying conformational asymmetry. Predicting $N_{B'C}/N_{AB}$ from Equation 2 requires a volume asymmetry α to use as a basis. For this basis, $\alpha = 1.48$ is a good choice because the same value has appeared in prior work as (i) the best volume asymmetry observed from SCFT in conformationally symmetric diblock alloys,[46] and (ii) the optimum volume asymmetry for Laves phases obtained from the unconstrained diblock foam model.[23] Figure 3 reveals two shortcomings in this estimate. First, the model fails to capture the effects of χN, consistently underestimating the chain length asymmetry for $\chi N = 28$. Such a failure makes sense when considering that the chains' radii of gyration will deviate more strongly from the ideal Gaussian estimate used in our derivation as segregation strength increases. Second, the model significantly underestimates the impact of ε_{AB}. However, when varying ε_{BC}, the model shows reasonable agreement with the observed value. Overall, the simple model of Equation 2 captures the $\chi N = 25$ behavior in Figs. 3b and 3c, but fails to capture the effects of segregation strength or accurately reflect the behavior in Fig. 3a.

We now continue our investigation with a thorough analysis of the phase behavior of the diblock alloy system with $N_{B'C}/N_{AB} = 1.0$, $\varepsilon_{AB} = 1.0$, and $\varepsilon_{BC} = 1.5$, identified prior to our discussion of Equation 2 as most effectively stabilizing the Laves phases amongst all of the systems we studied. To generate the phase diagram in Fig. 4, most phase boundaries were established first using the common-tangent construction[55] and canonical ensemble SCFT calculations. In addition to the C14, C15, fcc, bcc, and hex phases already described, 15 additional competitors were included in these calculations. The competing phases are inspired by a 2014 study of $B_1AB_2CB_3$ multiblock terpolymers by Xie *et al.*[59] and are identical to those chosen by Magruder *et al.*[46] for their block polymer alloys study. A list of all phases considered in the calculations is included in Table S1. Subsequent grand canonical calculations were used to resolve the region near each invariant point, where grand canonical ensemble's higher accuracy for problems involving macrophase separation[53] substantially benefits the identification of the three-phase coexistence at these points. Grand canonical calculations were also used to map the phase boundaries near the ODT, where both canonical SCFT calculations and common tangent calculations started to suffer from failed convergence. C14 was used to represent the Laves

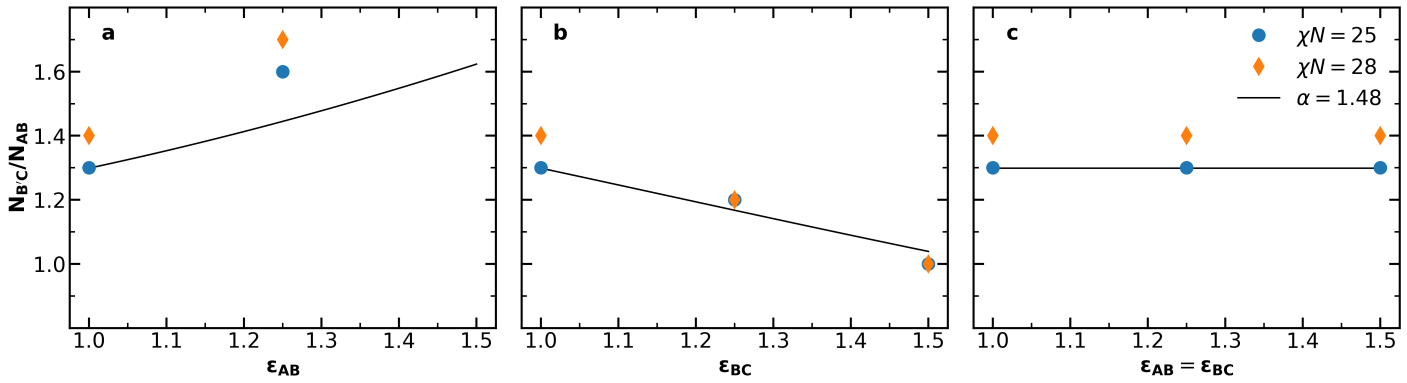

Fig. 3 The chain length asymmetry $N_{B'C}/N_{AB}$ at the F vs. $N_{B'C}/N_{AB}$ minima at $\chi N = 25$ (Fig. S2) and $\chi N = 28$ (Fig. 2), compared to the chain length asymmetry predicted by Equation 2 for $\alpha = 1.48$ when (a) ε_{AB} is varied, (b) ε_{BC} is varied, and (c) ε_{AB} and ε_{BC} are varied together. In (a), no minimum could be clearly observed for $\varepsilon_{AB} = 1.5$, as the lowest observed free energy occurred at $N_{B'C}/N_{AB} = 2.0$, which was the highest value considered.

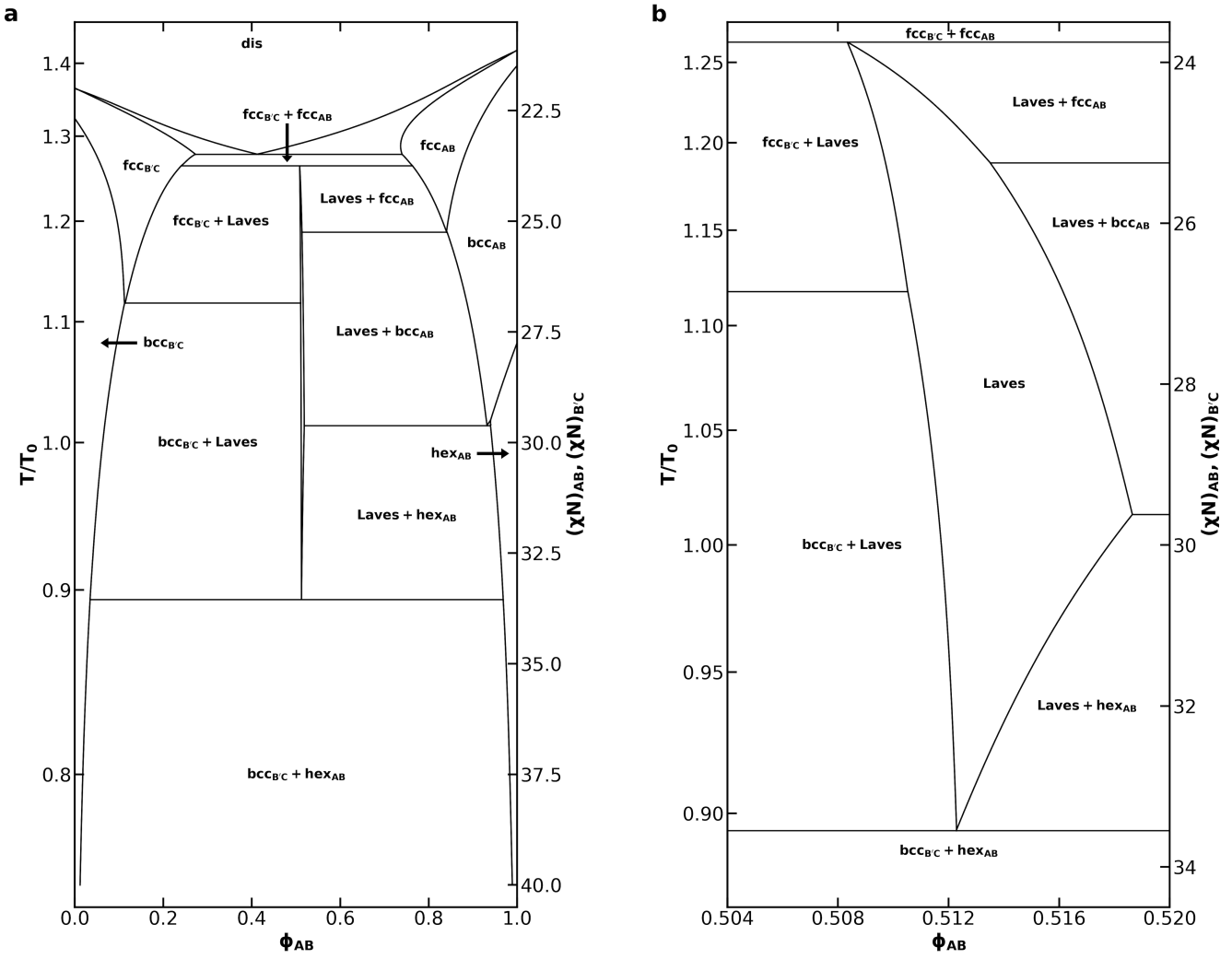

Fig. 4 (a) Phase diagram for an AB/B′C alloy with $N_{B'C}/N_{AB} = 1.0$, $f_A = f_C = 0.20$, $\varepsilon_{AB} = 1.0$, $\varepsilon_{BC} = 1.5$, and assuming purely enthalpic χ values such that $\chi_{AC}N_{AB} = 2(\chi N)$ at all T and (b) a detailed view of the Laves phase field within that phase diagram. The reference temperature, T_0, was chosen to correspond to $\chi N = 30$. Non-linear segments of the phase diagram are drawn using cubic splines fit to the sampled data. A companion phase diagram showing all of the points where SCFT calculations were performed is provided in Fig. S4.

phases while mapping the phase diagram. A detailed description of the canonical and grand canonical methodologies are included in the Supporting Information.

The phase diagram in Fig. 4a bears substantial qualitative resemblance to that presented by Magruder *et al.* for the conformationally symmetric case,[46] with many characteristics reminiscent of metal alloy phase diagrams. In each case, the diblock alloys display a eutectic transition from a disordered liquid to coexistence between AB-rich and B′C-rich fcc phases, as well as a peritectoid transition to a Laves phase field upon cooling from coexistence of simple sphere phases (fcc or bcc). In the conformationally asymmetric case, however, the temperature difference between the eutectic and peritectoid points is greatly reduced when compared to prior results for a conformationally symmetric system.[46] The peritectoid transitions of the two systems also differ on which simple sphere phase overtakes the Laves phase: bcc in the conformationally symmetric case,[46] and fcc here. As also noted by Magruder *et al.*,[46] experimental realization of this narrow eutectic to peritectoid transition is unlikely, given that fluctuation effects are expected to destroy the high-temperature regions of the diagram.

Below the peritectoid point, the Laves phase field widens as temperature decreases, and Laves coexistence with AB-rich and B′C-rich fcc phases is overtaken by coexistence with the corresponding bcc phases. At $\chi N = 28$, the highest segregation strength tested by Magruder *et al.*,[46] we find a Laves phase field with a width of 0.006 in ϕ_{AB}. This exceeds the 0.002 width in ϕ_{AB} reported previously,[46] consistent with the expectation that conformational asymmetry stabilizes Laves phases in the blend, while still possessing the narrow width characteristic of a phase field. The phase field reaches a maximum width at $\chi N = 29.62$ where the AB-rich bcc window closes, and the Laves phase starts to coexist with the AB-rich hex phase. At this segregation strength, the AB diblock would naturally form a hex phase in the neat melt. As the system is cooled further, conversion of the cylinder-forming AB diblock into spheres becomes increasingly unfavorable. The Laves phase field thus closes in a eutectoid transition to coexistence of B′C-rich bcc and AB-rich hex, which dominates the phase diagram at lower temperatures. The shape of the Laves phase field is difficult to resolve in Fig. 4a, so we include Fig. 4b to focus on the Laves window and help illuminate these details.

Compared to the neat melt conditions, both the AB-rich and B′C-rich fcc phase become stable over a much broader range of χN with the introduction of minority component. Aggregation of the minority component at the octahedral void of the structure has been shown to stabilize the fcc phases,[60,61] thus producing this effect. The difference in conformational asymmetry of the two diblocks results in substantial asymmetries in the phase diagram, particularly with regard to AB-rich and B′C-rich phase transitions. Conformational asymmetry shifts the phase boundaries of the neat B′C diblock relative to that of the AB diblock.[1,22,24–27] These morphological differences between the neat diblock melts carry over into the blended behavior, resulting in the asymmetries observed in Fig. 4. Of particular interest is the absence of any B′C-rich hex formation. The presence of hex on the AB-rich side of the diagram results in a rapid transition from a gradually broadening Laves phase field to a rapidly narrowing one.

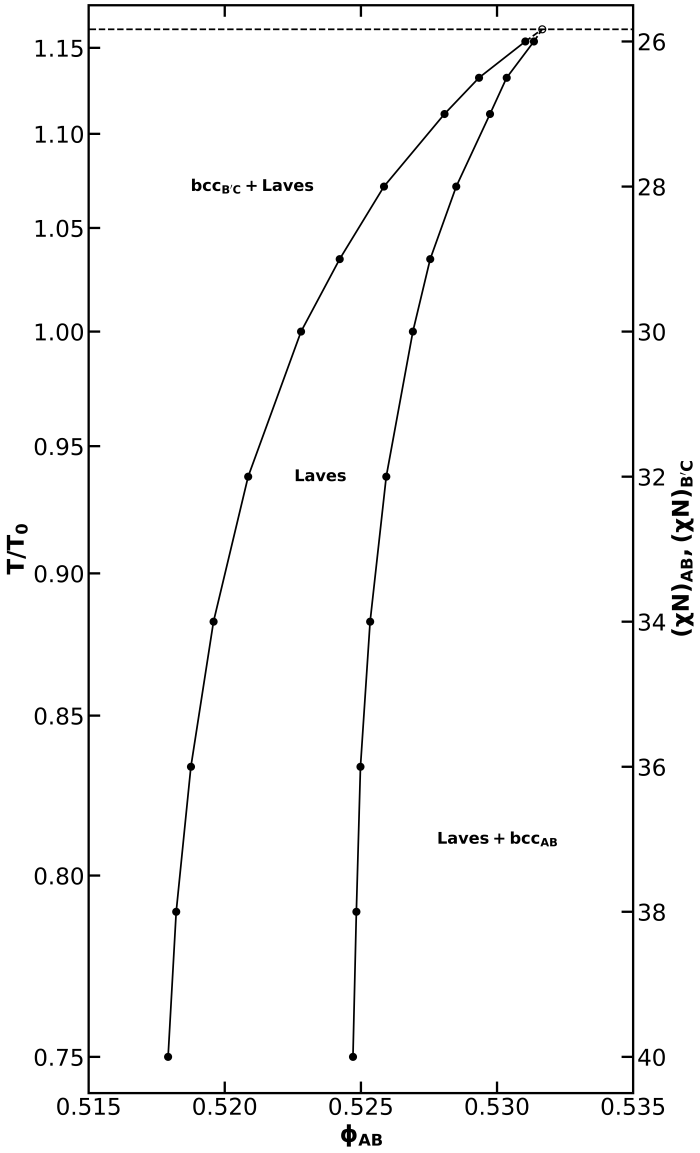

Fig. 5 The Laves phase window for $N_{\mathrm{B'C}}/N_{\mathrm{AB}} = 1.4$, $f_{\mathrm{A}} = f_{\mathrm{C}} = 0.20$, $\varepsilon_{\mathrm{AB}} = \varepsilon_{\mathrm{BC}} = 1.5$, and assuming purely enthalpic χ values such that $\chi_{\mathrm{AC}} N_{\mathrm{AB}} = 2(\chi N)$. The reference temperature T_0 was chosen to correspond to $\chi N = 30$. A peritectoid point and its associated tie line are included as a guide for the eye, but the position is interpolated from common-tangent data at $\chi N = 25.5$ and $\chi N = 26$, and are therefore marked with a dashed line and open data marker to reflect the imprecision of this estimate.

The narrowing of the Laves phase field at the AB-rich bcc-hex transition suggests that, without competition from hex phases, conformationally asymmetric binary diblock alloys may exhibit a Laves phase field out to strong segregation. In order to test this speculation, we need to select a system in which neither diblock undergoes a transition to hex in the neat melt. From Fig. 2c, we see that when both diblocks have a conformational asymmetry of 1.5, the Laves phase remains stable when the ratio of the degrees of polymerization is used to induce volume asymmetry. We also know that a neat diblock with $\varepsilon = 1.5$ and $f = 0.2$ will not assemble into hex below $\chi N = 40$,[25] which is an approximate upper bound for the ability to converge Frank-Kasper phase SCFT calcu-

lations with our software. Thus, we choose to further analyze an alloy system where $\varepsilon_{AB} = \varepsilon_{BC} = 1.5$ and $N_{B'C}/N_{AB} = 1.4$, which corresponds with the lowest relative free energy for Laves phases at the desired conformational asymmetry from our testing.

Using the same set of competing phases as for Fig. 4, the Laves phase field was mapped for this alloy. Canonical ensemble calculations were used in a common tangent analysis to identify the stable region for the Laves phase. As can be seen in Fig. 5, the Laves window remains open and continues to broaden up to $\chi N = 40$. The Laves window also shifts to lower ϕ_{AB} upon cooling, consistent with the trend seen in the work of Magruder *et al.* for conformationally symmetric alloys where $N_{B'C}/N_{AB}$ was also used to create distinct particle sizes.[46] It is also interesting to note that at the low-temperature end of Fig. 5, the AB-rich (right) side of the Laves window is much more nearly vertical than on the B′C-rich (left) side. Diblocks with the same block fraction and conformational asymmetry should exhibit the same phase behavior in the neat-melt limit; one might expect this symmetry to carry into the blending behavior and, likewise, into the Laves coexistence boundaries. However, both the deflection of the Laves window to lower ϕ_{AB} and the differing verticality of the coexistence boundaries demonstrate that this is not the case. This difference results from the asymmetry in chain length between the AB and B′C diblocks and resultant differences in their ability to pack in the interstitial sites of the bcc phases.

4 Conclusions

Using the Frank-Kasper Laves phases as a case study, we have demonstrated the ability of block polymer alloys to decouple the potentially competing effects of conformational asymmetry in different particle types, thereby probing the subtleties of its role in phase selection. In Laves phases, this decoupling revealed that increasing conformational asymmetry in the smaller, less spherical Laves particles has a detrimental effect on Laves phase stability, while increasing it in the larger, more spherical micelles is beneficial. The absence of significant changes to Laves stability when conformational asymmetry is simultaneously increased in both particles highlights how information can be obscured by competition when only a single conformational asymmetry is available – such as in a neat diblock melt.

Our results also demonstrate the value of independent conformational asymmetry control as a tool for designing self-assembling block polymer systems. Not only do we find that increasing conformational asymmetry in the large particles stabilizes the Laves phases, we also find that this effect is sufficient to produce the volume asymmetry required for Laves phase formation, without the need for asymmetry in the degrees of polymerization of the constituent chains, and results in a lower relative free energy for the Laves phases than was seen in the conformationally symmetric case. The phase diagram of this system bears a striking resemblance to that reported for the conformationally symmetric case,[46] with a slightly broader Laves window and a greater variety of phases coexisting with the Laves phase. With increasing segregation strength, increasing preference for cylinder formation by one of the diblocks causes cylinders to rapidly out-compete the Laves phases, thus closing the Laves phase field. We are further able to leverage conformational asymmetry to avoid this cylinder formation and stabilize the Laves phases out to high segregation strength, suggesting the potential to extend the Laves phase field out to the strong segregation limit by balancing chain composition, degrees of polymerization, and conformational asymmetries.

Based on the results presented here, and in prior work,[46] a substantial barrier to practical application of this methodology is likely to be the large windows of predicted macrophase separation. Introduction of some compatibilizing mechanism, such as hydrogen bonding between the corona blocks,[62] to favor greater contact between the distinct micelle types may further stabilize the Laves phase in an alloy-type blend. Although the literature on diblock copolymer alloys has so far focused on Laves phases, the methodology will likely find utility tuning individual domains in other Frank-Kasper phases or other morphologies, particularly if mechanisms can be found to reduce the size of macrophase separation windows.

Author Contributions

LJC, FSB, and KDD designed the research and edited the manuscript; LJC and KDD prepared the manuscript; LJC performed research and analyzed data.

Conflicts of interest

There are no conflicts to declare.

Acknowledgements

The authors thank Benjamin R. Magruder for helpful discussions and So Jung Park for valuable guidance regarding grand canonical ensemble methodologies. This work was supported by the National Science Foundation through DMR-1725272. Computational resources were provided in part by the Minnesota Supercomputing Institute.

Notes and references

1 S. T. Milner, *Macromolecules*, 1994, **27**, 2333–2335.
2 F. S. Bates and G. H. Fredrickson, *Macromolecules*, 1994, **27**, 1065–1067.
3 J. D. Vavasour and M. D. Whitmore, *Macromolecules*, 1993, **26**, 7070–7075.
4 M. W. Matsen and M. Schick, *Macromolecules*, 1994, **27**, 4014–4015.
5 G. M. Grason, *Phys. Rep.*, 2006, **433**, 1–64.
6 M. W. Matsen and M. Schick, *Phys. Rev. Lett.*, 1994, **72**, 2660–2663.
7 M. W. Matsen and F. S. Bates, *Macromolecules*, 1996, **29**, 1091–1098.
8 E. W. Cochran, C. J. Garcia-Cervera and G. H. Fredrickson, *Macromolecules*, 2006, **39**, 2449–2451.
9 L. Leibler, *Macromolecules*, 1980, **13**, 1602–1617.
10 F. S. Bates, R. E. Cohen and C. V. Berney, *Macromolecules*, 1982, **15**, 589–592.
11 E. L. Thomas, D. J. Kinning, D. B. Alward and C. S. Henkee, *Macromolecules*, 1987, **20**, 2934–2939.

12 A. N. Semenov, *Macromolecules*, 1989, **22**, 2849–2851.

13 Y.-Y. Huang, J.-Y. Hsu, H.-L. Chen and T. Hashimoto, *Macromolecules*, 2007, **40**, 406–409.

14 N.-W. Hsu, B. Nouri, L.-T. Chen and H.-L. Chen, *Macromolecules*, 2020, **53**, 9665–9675.

15 S. Lee, M. J. Bluemle and F. S. Bates, *Science*, 2010, **330**, 349–353.

16 N. Xie, W. Li, F. Qiu and A.-C. Shi, *ACS Macro Lett.*, 2014, **3**, 906–910.

17 K. Kim, M. W. Schulze, A. Arora, R. M. Lewis, M. A. Hillmyer, K. D. Dorfman and F. S. Bates, *Science*, 2017, **356**, 520–523.

18 M. W. Bates, J. Lequieu, S. M. Barbon, R. M. Lewis, K. T. Delaney, A. Anastasaki, C. J. Hawker, G. H. Fredrickson and C. M. Bates, *Proc. Natl. Acad. Sci. USA*, 2019, **116**, 13194–13199.

19 K. D. Dorfman, *Macromolecules*, 2021, **54**, 10251–10270.

20 F. C. Frank and J. S. Kasper, *Acta Crystallogr.*, 1958, **11**, 184–190.

21 F. C. Frank and J. S. Kasper, *Acta Crystallogr.*, 1959, **12**, 483–499.

22 G. M. Grason, B. A. DiDonna and R. D. Kamien, *Phys. Rev. Lett.*, 2003, **91**, 1–4.

23 A. Reddy, M. B. Buckley, A. Arora, F. S. Bates, K. D. Dorfman and G. M. Grason, *Proc. Natl. Acad. Sci. USA*, 2018, **115**, 10233–10238.

24 F. S. Bates, M. F. Schulz, A. K. Khandpur, S. Förster, J. H. Rosedale, K. Almdal and K. Mortensen, *Faraday Discuss.*, 1994, **98**, 7–18.

25 M. W. Matsen and F. S. Bates, *J. Polym. Sci. B: Polym. Phys.*, 1997, **35**, 945–952.

26 M. W. Matsen, *Macromolecules*, 2012, **45**, 2161–2165.

27 W. Li and Y.-X. Liu, *J. Chem. Phys.*, 2021, **154**, 014903.

28 P. D. Olmsted and S. T. Milner, *Phys. Rev. Lett.*, 1994, **72**, 936–939.

29 P. D. Olmsted and S. T. Milner, *Macromolecules*, 1998, **31**, 4011–4022.

30 R. P. Collanton and K. D. Dorfman, *Phys. Rev. Mater.*, 2022, **6**, 015602.

31 M. Dutour Sikirić, O. Delgado-Friedrichs and M. Deza, *Acta Crystallogr. A*, 2010, **66**, 602–615.

32 S. Lee, C. Leighton and F. S. Bates, *Proc. Natl. Acad. Sci. USA*, 2014, **111**, 17723–17731.

33 T. M. Gillard, S. Lee and F. S. Bates, *Proc. Natl. Acad. Sci. USA*, 2016, **113**, 5167–5172.

34 M. W. Schulze, R. M. Lewis, J. H. Lettow, R. J. Hickey, T. M. Gillard, M. A. Hillmyer and F. S. Bates, *Phys. Rev. Lett.*, 2017, **118**, 207801.

35 S. Jeon, T. Jun, S. Jo, H. Ahn, S. Lee, B. Lee and D. Y. Ryu, *Macromol. Rapid Commun.*, 2019, **40**, 1900259.

36 S. M. Barbon, J.-A. Song, D. Chen, C. Zhang, J. Lequieu, K. T. Delaney, A. Anastasaki, M. Rolland, G. H. Fredrickson, M. W. Bates, C. J. Hawker and C. M. Bates, *ACS Macro Lett.*, 2020, **9**, 1745–1752.

37 A. J. Mueller, A. P. Lindsay, A. Jayaraman, T. P. Lodge, M. K. Mahanthappa and F. S. Bates, *ACS Macro Lett.*, 2020, **9**, 576–582.

38 A. P. Lindsay, A. Jayaraman, A. J. Peterson, A. J. Mueller, S. Weigand, K. Almdal, M. K. Mahanthappa, T. P. Lodge and F. S. Bates, *ACS Nano*, 2021, **15**, 9453–9468.

39 K. Kim, A. Arora, R. M. Lewis, M. Liu, W. Li, A.-C. Shi, K. D. Dorfman and F. S. Bates, *Proc. Natl. Acad. Sci. USA*, 2018, **115**, 847–854.

40 B. Nouri, C.-Y. Chen, Y.-S. Huang, B. W. Mansel and H.-L. Chen, *Macromolecules*, 2021, **54**, 9195–9203.

41 A. P. Lindsay, G. K. Cheong, A. J. Peterson, S. Weigand, K. D. Dorfman, T. P. Lodge and F. S. Bates, *Macromolecules*, 2021, **54**, 7088–7101.

42 M. Liu, Y. Qiang, W. Li, F. Qiu and A.-C. Shi, *ACS Macro Lett.*, 2016, **5**, 1167–1171.

43 G. K. Cheong, F. S. Bates and K. D. Dorfman, *Proc. Natl. Acad. Sci. USA*, 2020, **117**, 16764–16769.

44 J. Xie and A.-C. Shi, *Giant*, 2021, **5**, 100043.

45 A. P. Lindsay, A. J. Mueller, M. K. Mahanthappa, T. P. Lodge and F. S. Bates, *Wigner-Seitz Cell generation and calculations in MATLAB*, 2021, Retrieved from the Data Repository for the University of Minnesota.

46 B. R. Magruder, S. J. Park, R. P. Collanton, F. S. Bates and K. D. Dorfman, *Macromolecules*, 2022, **55**, 2991–2998.

47 E. Helfand, *J. Chem. Phys.*, 1975, **62**, 999–1005.

48 E. Helfand, *Macromolecules*, 1975, **8**, 552–556.

49 F. Stein and A. Leineweber, *J. Mater. Sci.*, 2021, **56**, 5321–5427.

50 M. W. Matsen, *J. Phys. Condens. Mat.*, 2002, **14**, R21–R47.

51 G. H. Fredrickson, *The Equilibrium Theory of Inhomogeneous Polymers*, Oxford University Press, Oxford, United Kingdom, 2006.

52 G. K. Cheong, A. Chawla, D. C. Morse and K. D. Dorfman, *Eur. Phys. J. E*, 2020, **43**, 15.

53 M. W. Matsen, *Phys. Rev. Lett.*, 1995, **74**, 4225–4228.

54 A. Shi, *Variational Methods in Molecular Modeling*, Springer Singapore, Singapore, 2017, pp. 155–180.

55 M. D. Whitmore and J. Noolandi, *Macromolecules*, 1985, **18**, 2486–2497.

56 B. R. Magruder and K. D. Dorfman, *Soft Matter*, 2021, **17**, 8950–8959.

57 M. H. Uddin, C. Rodriguez, A. López-Quintela, D. Leisner, C. Solans, J. Esquena and H. Kunieda, *Macromolecules*, 2003, **36**, 1261–1271.

58 M. Zhao and W. Li, *Macromolecules*, 2019, **52**, 1832–1842.

59 N. Xie, M. Liu, H. Deng, W. Li, F. Qiu and A.-C. Shi, *J. Am. Chem. Soc.*, 2014, **136**, 2974–2977.

60 L. Chen, Y. Qiang and W. Li, *Macromolecules*, 2018, **51**, 9890–9900.

61 M. W. Matsen, *Phys. Rev. Lett.*, 2007, **99**, 148304.

62 Q. Li, D. Woo, J.-K. Kim and W. Li, *Macromolecules*, 2022, **55**, 6525–6535.

Supporting information for: Tunable conformational asymmetry in particle-forming diblock copolymer alloys

Logan J. Case, Frank S. Bates, and Kevin D. Dorfman*

Department of Chemical Engineering and Materials Science, University of Minnesota – Twin Cities, 421 Washington Ave SE, Minneapolis, Minnesota 55455, United States

E-mail: dorfman@umn.edu

*To whom correspondence should be addressed

Contents

S1 Self-Consistent Field Theory

Calculations in this work are performed using the C++ implementation of the Polymer Self-Consistent Field (PSCFpp) software package.[S1] In this section, we present the formulation of the block copolymer self-consistent mean field theory (SCFT) implemented in PSCFpp. Our discussion here closely follows the formalism presented alongside PSCFpp's Fortran-based predecessor,[S2,S3] although the present discussion is specific to the diblock alloy system. More generalized discussions of SCFT are available elsewhere.[S4–S6]

Using PSCFpp, we consider a system of incompressible, continuous Gaussian chain polymers composed of three unique monomer types $i \in \{\mathrm{A}, \mathrm{B}, \mathrm{C}\}$, with statistical segment lengths b_i. These monomers are coarse-grained and occupy the common monomer reference volume v. The interaction strength between two monomers i and $j \neq i$ is given by the Flory-Huggins parameter χ_{ij}; self-interaction of a monomer i with itself is thermodynamically neutral with $\chi_{ii} = 0$. We consider a blend of two diblock polymer chains $k \in \{\mathrm{AB}, \mathrm{B'C}\}$ with total chain degrees of polymerization N_{AB} for the AB chain and $N_{\mathrm{B'C}}$ for the B′C chain. These total degrees of polymerization represent the sum of the degrees of polymerization of their constituent blocks such that $N_{\mathrm{AB}} = N_{\mathrm{A}} + N_{\mathrm{B}}$ is the sum of N_{A} A-monomers and N_{B} B-monomers while $N_{\mathrm{B'C}} = N_{\mathrm{B'}} + N_{\mathrm{C}}$ is the sum of $N_{\mathrm{B'}}$ B-monomers and N_{C} C-monomers. In the blend, the overall volume fractions of the AB and B′C polymers are ϕ_{AB} and $\phi_{\mathrm{B'C}} = 1 - \phi_{\mathrm{AB}}$, respectively. The requirement of a uniform coarse-grained monomer volume v yields an equivalence between volume and degree of polymerization such that the volume fraction of a block within a polymer chain is given by its degree of polymerization: $f_{\mathrm{A}} = N_{\mathrm{A}}/N_{\mathrm{AB}}$ for the A-block in the AB chain and $f_{\mathrm{C}} = N_{\mathrm{C}}/N_{\mathrm{B'C}}$ for the C-block in the B′C chain. SCFT calculations in PSCFpp are performed on a single unit-cell with periodic boundary conditions to represent the structure throughout a macroscopic volume. This unit cell has volume V and contains $n = V/v$ monomers.

It is useful to note that, in the context of SCFT calculations in PSCFpp, a "monomer" acts as a bookkeeping device and there is far more flexibility in its definition than would be

appropriate in a synthetic or experimental context. In the SCFT formalism, a "monomer" need not represent a single chemical repeat unit, as is typical in a synthetic context, but instead represents the molar mass of polymer chain occupying one monomer reference volume, v.[S3] In our calculations, v is chosen such that $N_{\mathrm{AB}} = 1$ which produces two convenient outcomes. First, chain length asymmetry, $N_{\mathrm{B'C}}/N_{\mathrm{AB}}$, becomes numerically equivalent to $N_{\mathrm{B'C}}$. Second, energies can be easily reported on a per-chain basis because the number of monomers in the system, n, can be interpreted as the number of chains of length N_{AB}. Sinturel et al.[S7] offer a helpful discussion about mapping the SCFT parameters to those of real polymers.

In SCFT, the many-body particle-particle interactions of the polymer melt are replaced by a spatially varying chemical potential field acting on a representative set of non-interacting polymer chains in the saddle-point approximation that is relevant as a mean-field description. The potential field acting on monomer i at spatial position $\mathbf{r}$ is denoted by $\omega_i(\mathbf{r})$ and given for each monomer by

$$\omega_{\mathrm{A}}(\mathbf{r}) = \chi_{\mathrm{AB}}\rho_{\mathrm{B}}(\mathbf{r}) + \chi_{\mathrm{AC}}\rho_{\mathrm{C}}(\mathbf{r}) + \xi(\mathbf{r}) \tag{S1}$$

$$\omega_{\mathrm{B}}(\mathbf{r}) = \chi_{\mathrm{AB}}\rho_{\mathrm{A}}(\mathbf{r}) + \chi_{\mathrm{BC}}\rho_{\mathrm{C}}(\mathbf{r}) + \xi(\mathbf{r}) \tag{S2}$$

$$\omega_{\mathrm{C}}(\mathbf{r}) = \chi_{\mathrm{AC}}\rho_{\mathrm{A}}(\mathbf{r}) + \chi_{\mathrm{BC}}\rho_{\mathrm{B}}(\mathbf{r}) + \xi(\mathbf{r}) \tag{S3}$$

where $\rho_i(\mathbf{r})$ is the average local volume fraction of monomer i at position $\mathbf{r}$ and $\xi(\mathbf{r})$ is a Lagrange multiplier enforcing the incompressibility constraint,

$$\rho_{\mathrm{A}}(\mathbf{r}) + \rho_{\mathrm{B}}(\mathbf{r}) + \rho_{\mathrm{C}}(\mathbf{r}) = 1 \tag{S4}$$

Running an SCFT calculation requires that the user first provide an initial guess for ω_{A}, ω_{B}, and ω_{C}. These initial values are used to compute the partition function of each polymer

k according to

$$Q_k = \frac{1}{V}\int_V d\mathbf{r}\, q_k(\mathbf{r}, N_k) \tag{S5}$$

where the forward propagator $q_k(\mathbf{r}, N_k)$ represents the solution of the modified diffusion initial value problem for chain type k,

$$\frac{\partial q_k(\mathbf{r}, s)}{\partial s} = \left[\frac{b_{i(s)}^2}{6}\nabla^2 - \omega_{i(s)}(\mathbf{r})\right] q_k(\mathbf{r}, s), \qquad q_k(\mathbf{r}, 0) = 1 \tag{S6}$$

where $s \in [0, N_k]$ is the coordinate along the chain contour. The subscript $i(s)$ on $b_{i(s)}$ and $\omega_{i(s)}$ indicate that the statistical segment length and chemical potential field will be those corresponding to the monomer type at contour position s. More explicitly: when $k = \mathrm{AB}$, we use b_A and $\omega_\mathrm{A}(\mathbf{r})$ when integrating over the region $s \in [0, N_\mathrm{A}]$ and we use b_B and $\omega_\mathrm{B}(\mathbf{r})$ for integration over $s \in [N_\mathrm{A}, N_\mathrm{AB}]$; when $k = \mathrm{B'C}$, we use b_C and $\omega_\mathrm{C}(\mathbf{r})$ for integration over $s \in [0, N_\mathrm{C}]$ and we use b_B and $\omega_\mathrm{B}(\mathbf{r})$ for integration over $s \in [N_\mathrm{C}, N_\mathrm{B'C}]$.

The forward propagator $q_k(\mathbf{r}, s)$ is a normalized partition function for the portion of chain k on $[0, s]$ when the chain contour segment s is constrained to position $\mathbf{r}$. Under the same positional constraint of segment s, the normalized partition function for the remainder of chain k, $[s, N_k]$, is given by the backward propagator $q_k^\dagger(\mathbf{r}, s)$ which is the solution of the modified diffusion initial value problem

$$-\frac{\partial q_k^\dagger(\mathbf{r}, s)}{\partial s} = \left[\frac{b_{i(s)}^2}{6}\nabla^2 - \omega_{i(s)}(\mathbf{r})\right] q_k^\dagger(\mathbf{r}, s), \qquad q_k^\dagger(\mathbf{r}, N_k) = 1 \tag{S7}$$

The product of the forward and backward propagators, $q_k(\mathbf{r}, s)q_k^\dagger(\mathbf{r}, s)$, is proportional to the probability of finding chain contour segment s at position $\mathbf{r}$.[S4] This proportionality can then be used to compute the average local volume fractions of each monomer, $\rho_i(\mathbf{r})$, which in turn can be used to compute the potential field for each monomer $\omega_i(\mathbf{r})$. Details of the local monomer volume fractions differ between the canonical and grand canonical ensembles, and are given below in Equations S8-S9 and S13-S14 respectively.

The circular dependence of Equations S1-S3 on Equations S8-S10 (or Equations S13-S15) via Equations S4-S7 means that the SCFT calculation must iterate on $\omega_i(\mathbf{r})$ from the user-provided initial guess until these equations become self-consistent within a specified tolerance. In our calculations, we measure error using the relative residual norm described by Matsen[S8] and converge calculations to a tolerance of 1×10^{-6}. Iterations are done according to an Anderson Mixing scheme[S8–S10] which optimizes unit cell parameters simultaneously with the field[S10,S11] to minimize stress and obtain an accurate free energy.

S1.1 Canonical Ensemble

In the canonical ensemble, system composition is specified for the system by declaring ϕ_{AB} and $\phi_{\mathrm{B'C}}$ in the input file. Using these values, and the partition functions above, the local volume fractions of each monomer are calculated with[S6]

$$\rho_{\mathrm{A}}(\mathbf{r}) = \frac{\phi_{\mathrm{AB}}}{Q_{\mathrm{AB}} N_{\mathrm{AB}}} \int_0^{N_{\mathrm{A}}} ds\, q_{\mathrm{AB}}(\mathbf{r}, s) q^{\dagger}_{\mathrm{AB}}(\mathbf{r}, s) \tag{S8}$$

$$\rho_{\mathrm{B}}(\mathbf{r}) = \frac{\phi_{\mathrm{AB}}}{Q_{\mathrm{AB}} N_{\mathrm{AB}}} \int_{N_{\mathrm{A}}}^{N_{\mathrm{AB}}} ds\, q_{\mathrm{AB}}(\mathbf{r}, s) q^{\dagger}_{\mathrm{AB}}(\mathbf{r}, s) + \frac{\phi_{\mathrm{B'C}}}{Q_{\mathrm{B'C}} N_{\mathrm{B'C}}} \int_{N_{\mathrm{C}}}^{N_{\mathrm{B'C}}} ds\, q_{\mathrm{B'C}}(\mathbf{r}, s) q^{\dagger}_{\mathrm{B'C}}(\mathbf{r}, s) \tag{S9}$$

$$\rho_{\mathrm{C}}(\mathbf{r}) = \frac{\phi_{\mathrm{B'C}}}{Q_{\mathrm{B'C}} N_{\mathrm{B'C}}} \int_0^{N_{\mathrm{C}}} ds\, q_{\mathrm{B'C}}(\mathbf{r}, s) q^{\dagger}_{\mathrm{B'C}}(\mathbf{r}, s) \tag{S10}$$

After these equations are solved self-consistently with those in Equations S1-S7, the Helmholtz free energy per monomer is given by[S2]

$$\begin{aligned} \frac{F}{n k_B T} = \frac{1}{V} \int d\mathbf{r} \left[(\chi_{\mathrm{AB}} \rho_{\mathrm{A}} \rho_{\mathrm{B}} + \chi_{\mathrm{AC}} \rho_{\mathrm{A}} \rho_{\mathrm{C}} + \chi_{\mathrm{BC}} \rho_{\mathrm{B}} \rho_{\mathrm{C}}) - (\omega_{\mathrm{A}} \rho_{\mathrm{A}} + \omega_{\mathrm{B}} \rho_{\mathrm{B}} + \omega_{\mathrm{C}} \rho_{\mathrm{C}}) \right] \\ + \frac{\phi_{\mathrm{AB}}}{N_{\mathrm{AB}}} \left(\ln \frac{\phi_{\mathrm{AB}}}{Q_{\mathrm{AB}}} - 1 \right) + \frac{\phi_{\mathrm{B'C}}}{N_{\mathrm{B'C}}} \left(\ln \frac{\phi_{\mathrm{B'C}}}{Q_{\mathrm{B'C}}} - 1 \right) \end{aligned} \tag{S11}$$

where $k_B T$ is the Boltzmann constant and T is the absolute temperature.

S1.2 Grand Canonical Ensemble

Instead of system composition, calculations in the grand canonical ensemble specify the dimensionless chemical potential of the AB and B′C polymers (μ_{AB}/k_BT and $\mu_{\mathrm{B'C}}/k_BT$, respectively). These chemical potentials are related to the overall volume fractions by[S6]

$$\exp\left(\frac{\mu_k}{k_BT}\right)Q_k = \phi_k \tag{S12}$$

This relation, combined with incompressibility of the system, means that μ_{AB}/k_BT and $\mu_{\mathrm{B'C}}/k_BT$ are not independent, allowing us to set $\mu_{\mathrm{AB}}/k_BT = 0$ throughout our calculations while varying $\mu_{\mathrm{B'C}}/k_BT$. The relation in Equation S12 can also be used to compute the local volume fractions of each monomer via substitution into Equations S8-S10, giving

$$\rho_{\mathrm{A}}(\mathbf{r}) = \frac{1}{N_{\mathrm{A}}}\exp\left(\frac{\mu_{\mathrm{AB}}}{k_BT}\right)\int_0^{N_{\mathrm{A}}} ds\; q_{\mathrm{AB}}(\mathbf{r},s)q^{\dagger}_{\mathrm{AB}}(\mathbf{r},s) \tag{S13}$$

$$\begin{aligned}\rho_{\mathrm{B}}(\mathbf{r}) = {} & \frac{1}{N_{\mathrm{AB}}}\exp\left(\frac{\mu_{\mathrm{AB}}}{k_BT}\right)\int_{N_{\mathrm{A}}}^{N_{\mathrm{AB}}} ds\; q_{\mathrm{AB}}(\mathbf{r},s)q^{\dagger}_{\mathrm{AB}}(\mathbf{r},s) \\ & + \frac{1}{N_{\mathrm{B'C}}}\exp\left(\frac{\mu_{\mathrm{B'C}}}{k_BT}\right)\int_{N_{\mathrm{C}}}^{N_{\mathrm{B'C}}} ds\; q_{\mathrm{B'C}}(\mathbf{r},s)q^{\dagger}_{\mathrm{B'C}}(\mathbf{r},s)\end{aligned} \tag{S14}$$

$$\rho_{\mathrm{C}}(\mathbf{r}) = \frac{1}{N_{\mathrm{B'C}}}\exp\left(\frac{\mu_{\mathrm{B'C}}}{k_BT}\right)\int_0^{N_{\mathrm{C}}} ds\; q_{\mathrm{B'C}}(\mathbf{r},s)q^{\dagger}_{\mathrm{B'C}}(\mathbf{r},s) \tag{S15}$$

After the calculation converges, the grand canonical free energy is given by[S12]

$$F_g = -PV \tag{S16}$$

where P is the system pressure. For our alloy system, the number of AB chains, n_{AB}, and the number of B′C chains, $n_{\mathrm{B'C}}$, along with their respective chemical potentials can be used to relate the grand canonical free energy to the Helmholtz free energy with[S6]

$$F_g = F - n_{\mathrm{AB}}\mu_{\mathrm{AB}} - n_{\mathrm{B'C}}\mu_{\mathrm{B'C}} \tag{S17}$$

which can be combined with Equation S16 to give

$$PV = -F + n_{\mathrm{AB}}\mu_{\mathrm{AB}} + n_{\mathrm{B'C}}\mu_{\mathrm{B'C}} \tag{S18}$$

By noting that $n_k = n\phi_k/N_k$ and non-dimensionalizing Equation S18 by dividing by nk_BT, we obtain

$$\frac{Pv}{k_BT} = -\frac{F}{nk_BT} + \frac{\phi_{\mathrm{AB}}}{N_{\mathrm{AB}}}\left(\frac{\mu_{\mathrm{AB}}}{k_BT}\right) + \frac{\phi_{\mathrm{B'C}}}{N_{\mathrm{B'C}}}\left(\frac{\mu_{\mathrm{B'C}}}{k_BT}\right) \tag{S19}$$

which gives the dimensionless pressure output by PSCFpp in terms of the dimensionless chemical potentials, dimensionless Helmholtz free energy, and overall species volume fractions, all of which are also reported by the program.[S3]

S2 Phase Coexistence

For two or more phases to be in equilibrium, they must have equal pressure and temperature, and the chemical potential of each species in the system must be the same in all phases. In the SCFT calculations employed here, the temperature of the system is set by the Flory-Huggins parameter χ_{ij}; therefore, the equal temperature condition for equilibrium is met as long as calculations are done at fixed χ_{ij}, regardless of the ensemble in which calculations are performed. Establishing the equal-pressure and equal-chemical potential conditions differs by the ensemble selected. The remainder of this section describes the methods for equilibrium determination in the canonical and grand canonical ensembles.

S2.1 Canonical Ensemble: Common Tangent

The SCFT calculations performed here assume incompressibility of the polymers. Due to this assumption in the canonical ensemble, the addition of a constant pressure to the system will not change the Helmholtz free energy.[S6] This means that the pressure in the canonical ensemble is arbitrary, and the requirement of constant pressure can always be met. The

requirement of equal chemical potential in all phases for each species is established via the common tangent construction.[S13]

To numerically determine a common tangent between phases I and II, the Helmholtz free energy data for each phase, collected at intervals of $\Delta\phi_{\mathrm{AB}} = 0.005$, is first fit to a cubic spline, giving the energy of each phase as a function of ϕ_{AB}, $F^{\mathrm{I}}(\phi_{\mathrm{AB}})$ and $F^{\mathrm{II}}(\phi_{\mathrm{AB}})$. To ensure fidelity to the underlying data, this spline was computed with a zero smoothing factor, which forces the curve to pass exactly through all data points.[S14] The compositions of the two coexisting phases, $\phi^{\mathrm{I}}_{\mathrm{AB}}$ and $\phi^{\mathrm{II}}_{\mathrm{AB}}$, were then calculated numerically by seeking the root of

$$\mathbf{f}(\phi^{\mathrm{I}}_{\mathrm{AB}}, \phi^{\mathrm{II}}_{\mathrm{AB}}) = \begin{bmatrix} f_1(\phi^{\mathrm{I}}_{\mathrm{AB}}, \phi^{\mathrm{II}}_{\mathrm{AB}}) \\ f_2(\phi^{\mathrm{I}}_{\mathrm{AB}}, \phi^{\mathrm{II}}_{\mathrm{AB}}) \end{bmatrix} \tag{S20}$$

where f_1 and f_2 are given by

$$f_1(\phi^{\mathrm{I}}_{\mathrm{AB}}, \phi^{\mathrm{II}}_{\mathrm{AB}}) = \frac{dF^{\mathrm{I}}}{d\phi_{\mathrm{AB}}}(\phi^{\mathrm{I}}_{\mathrm{AB}}) - \frac{F^{\mathrm{I}}(\phi^{\mathrm{I}}_{\mathrm{AB}}) - F^{\mathrm{II}}(\phi^{\mathrm{II}}_{\mathrm{AB}})}{\phi^{\mathrm{I}}_{\mathrm{AB}} - \phi^{\mathrm{II}}_{\mathrm{AB}}} \tag{S21}$$

$$f_2(\phi^{\mathrm{I}}_{\mathrm{AB}}, \phi^{\mathrm{II}}_{\mathrm{AB}}) = \frac{dF^{\mathrm{II}}}{d\phi_{\mathrm{AB}}}(\phi^{\mathrm{I}}_{\mathrm{AB}}) - \frac{F^{\mathrm{I}}(\phi^{\mathrm{I}}_{\mathrm{AB}}) - F^{\mathrm{II}}(\phi^{\mathrm{II}}_{\mathrm{AB}})}{\phi^{\mathrm{I}}_{\mathrm{AB}} - \phi^{\mathrm{II}}_{\mathrm{AB}}} \tag{S22}$$

The root of $\mathbf{f}(\phi^{\mathrm{I}}_{\mathrm{AB}}, \phi^{\mathrm{II}}_{\mathrm{AB}})$ occurs when the slope of the tangent to each energy curve, $dF^i/d\phi_{\mathrm{AB}}$, is equal to the slope of the line connecting the two tangent points, $\left(\phi^{\mathrm{I}}_{\mathrm{AB}}, F^{\mathrm{I}}(\phi^{\mathrm{I}}_{\mathrm{AB}})\right)$ and $\left(\phi^{\mathrm{II}}_{\mathrm{AB}}, F^{\mathrm{II}}(\phi^{\mathrm{II}}_{\mathrm{AB}})\right)$, which guarantees that the points are co-linear along the common tangent. This construction is depicted in Fig. S1.

Optimization was done with the SciPy root-finding method `scipy.optimize.root` using the `'hybr'` method option, which uses a modified Powell method as implemented in MINPACK.[S15,S16] In general, we find this method to be very robust for common tangent calculations, with most tangent calculations converging when the mid-point of each energy curve is used as the initial guess for the respective ϕ^i_{AB}, which was the default initial guess for our calculations.

When this methodology was used to choose a macrophase separation pairing for com-

parison to the Laves phase, as done in Fig. S2 or Fig. 2 of the main text, phases I and II represent the AB-rich and B′C-rich bcc or fcc phases. This same methodology was used in construction of the phase diagram to determine phase boundaries along the Laves phase field, in which case phases I and II would represent a Laves phase and one of the AB-rich or B′C-rich phases.

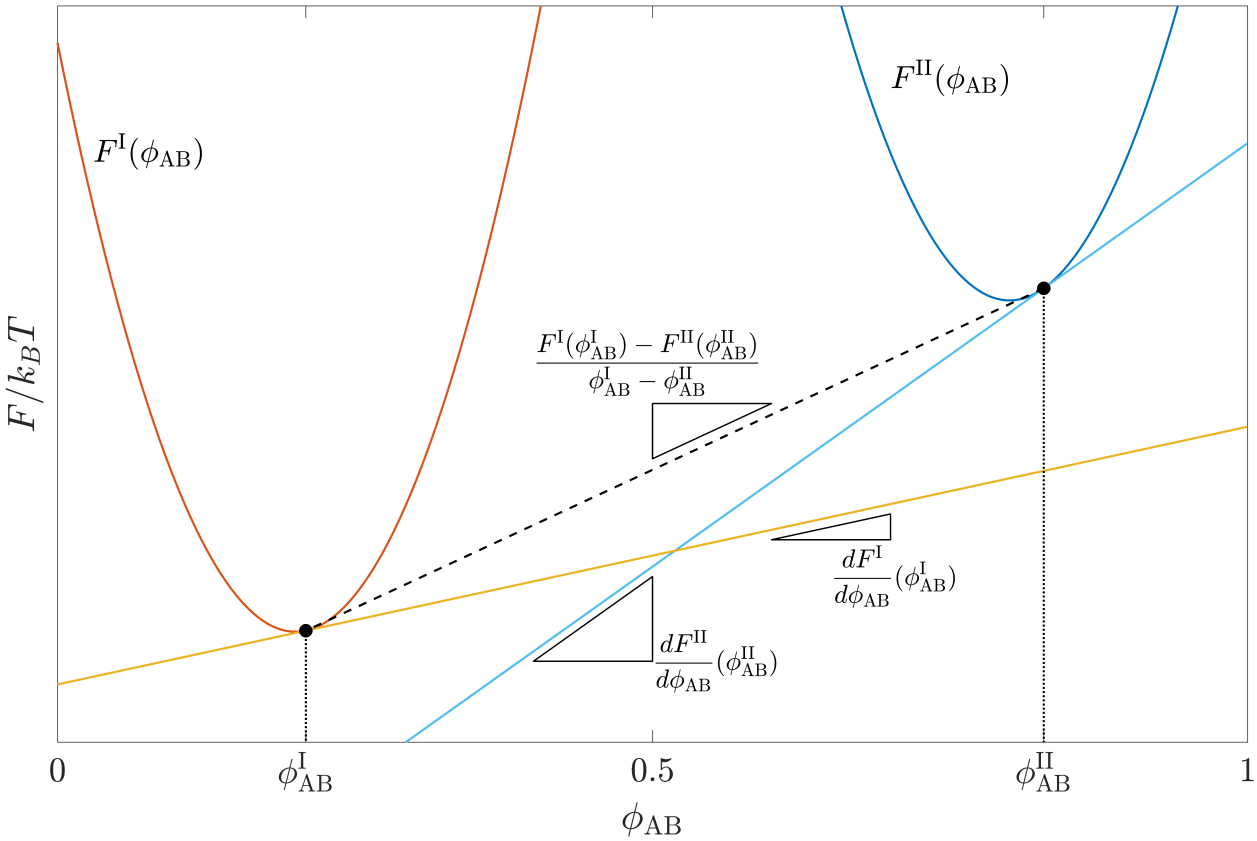

Figure S1: Representative illustration of the common tangent calculation method for arbitrary phases I and II, using hypothetical quadratic Helmholtz free energy curves for these phases, $F^{\mathrm{I}}(\phi_{\mathrm{AB}})$ and $F^{\mathrm{II}}(\phi_{\mathrm{AB}})$ respectively. The method iterates on the values of the coexistence compositions, $\phi^{\mathrm{I}}_{\mathrm{AB}}$ (phase I) and $\phi^{\mathrm{II}}_{\mathrm{AB}}$ (phase II), to find the root of Equation S20. The solid lines are the tangents to $F^{\mathrm{I}}(\phi_{\mathrm{AB}})$ and $F^{\mathrm{II}}(\phi_{\mathrm{AB}})$ at the points $\left(\phi^{\mathrm{I}}_{\mathrm{AB}}, F^{\mathrm{I}}(\phi^{\mathrm{I}}_{\mathrm{AB}})\right)$ and $\left(\phi^{\mathrm{II}}_{\mathrm{AB}}, F^{\mathrm{II}}(\phi^{\mathrm{II}}_{\mathrm{AB}})\right)$, respectively. These tangent points are marked with black dots. The dashed line connects the two tangent points, $\left(\phi^{\mathrm{I}}_{\mathrm{AB}}, F^{\mathrm{I}}(\phi^{\mathrm{I}}_{\mathrm{AB}})\right)$ and $\left(\phi^{\mathrm{II}}_{\mathrm{AB}}, F^{\mathrm{II}}(\phi^{\mathrm{II}}_{\mathrm{AB}})\right)$. The slopes of the tangent lines and the connector line are indicated on the graph algebraically as they are listed in Equations S21 and S22. When all three slopes are equal, at the root of Equation S20, the tangent points $\left(\phi^{\mathrm{I}}_{\mathrm{AB}}, F^{\mathrm{I}}(\phi^{\mathrm{I}}_{\mathrm{AB}})\right)$ and $\left(\phi^{\mathrm{II}}_{\mathrm{AB}}, F^{\mathrm{II}}(\phi^{\mathrm{II}}_{\mathrm{AB}})\right)$ will be co-linear along the common tangent.

S2.2 Grand Canonical Ensemble

Our approach to phase coexistence in the grand canonical ensemble follows the method described by Matsen [S17] and that used by Magruder et al. [S18] in their work on conformationally symmetric diblock alloys. Due to the incompressibility of the system, the chemical potentials of the AB and B′C chains are not independent, allowing us to choose $\mu_{\mathrm{AB}}/k_BT = 0$ for all calculations. This trivially satisfies the chemical potential criteria for the AB chain. The chemical potential value input to PSCF for the B′C chain, $\mu_{\mathrm{B'C}}/k_BT$, is then controlled as an independent variable and phases are compared across $\mu_{\mathrm{B'C}}/k_BT$ values (similarly to ϕ_{AB} in the canonical ensemble). By controlling the value of $\mu_{\mathrm{B'C}}/k_BT$, we thus also meet the chemical potential criterion for B′C. The pressure of each phase as calculated with Eqn. S19 is output by PSCF following convergence of the SCFT calculation. The final equilibrium criterion, equal pressure, is met when the Pv/k_BT vs $\mu_{\mathrm{B'C}}/k_BT$ curves of the phases intersect. In general, SCFT calculations were run at increments of 0.0005 in $\mu_{\mathrm{B'C}}/k_BT$. In some cases, however, larger sampling increments were required when large ranges of $\mu_{\mathrm{B'C}}/k_BT$ needed to be sampled to find an intercept. These larger sampling increments were most often needed while resolving the high-temperature regions near the ODT, where the $P(\mu_{\mathrm{B'C}})$ curves of disorder and the AB-rich or B′C-rich fcc phases were nearly parallel. In these cases, $\mu_{\mathrm{B'C}}/k_BT$ needed to be sampled over ranges up to two orders of magnitude larger than was typically required. Regardless of sampling increment, interpolation was used to determine the chemical potential and composition of the phases at equilibrium.

S3 Impact of Conformational Asymmetry

As discussed in the main text, we evaluated the impact of conformational asymmetry in each of the Laves particles by simultaneously varying the chain length asymmetry and the conformational asymmetries. At each condition conformational asymmetry and chain length asymmetry, we ran canonical ensemble SCFT calculations at a variety of blend fractions for

the Laves phases and a set of AB-rich and B′C-rich macrophase separation competitors. We used the common tangent construction to determine which set of AB-rich and B′C-rich phases made the most competitive macrophase separation pair, and compared the Laves phase energy to this macrophase separation tangent. The results of this analysis at $\chi N = 28.0$ were reported in Figure 2 of the main text. Figure S2 reports the results of this analysis at $\chi N = 25.0$. Unlike at $\chi N = 28$, where bcc-bcc coexistence dominated the macrophase separation reference, here both fcc and bcc appear frequently on both ends of the macrophase separation tangent. Aside from the more frequent appearance of fcc phases, the trends seen here are quite similar to those reported in the main text.

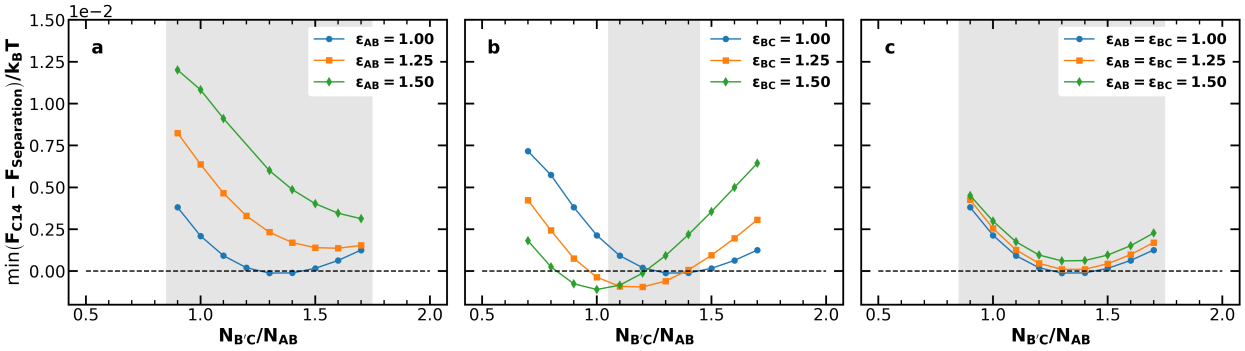

Figure S2: Minimum free energy of the C14 Laves phase relative to the macrophase separation tangent line at various conformational asymmetries for (a) the AB diblock, (b) the B′C diblock, or (c) both the AB and B′C diblocks for $\chi_{AB}N_{AB} = \chi_{BC}N_{B'C} = 25.0$, $\chi_{AC}N_{AB} = 50.0$, and $f_A = f_C = 0.20$. Shaded regions indicate those in which one or both of the AB-rich and B′C-rich fcc phases are used in the macrophase separation tangent (in place of the corresponding bcc phase) at one or more of the conformational asymmetries studied here.

S4 Candidate Phases

In order to generate the phase diagrams reported in the main text, we needed to consider a variety of competitor phases in addition to the Laves phases and macrophase separation candidates. Table S1 lists the phases considered during construction of phase diagrams. The table contains crystallographic information, SCFT spatial discretization, and information on

the number of particles and assignment of particles as AB or B′C micelles. As stated in the main text, the phases considered in this work are inspired by the work of Xie et al.[S19] and match the candidate set employed by Magruder et al.[S18] In constructing our phase diagram, we have chosen to omit hexagonally close-packed spheres (hcp) from the set of candidate phases. The hcp phase is nearly degenerate with fcc,[S19,S20] and any changes (if any) it would produce in the phase diagram would be negligible; fcc is taken to be representative of both close-packed sphere phases.

Several of the candidate phases listed here (specifically ReO_3, TiO_2, CaF_2, and α-Al_2O_3) proved particularly difficult to converge in many regions of the phase diagram, as noted previously by Magruder et al.,[S18] and are therefore missing from many of the canonical ensemble calculation sets. Among these phases, ReO_3 proved the most problematic, as we were unable to achieve convergence of an initial field at the desired conformational asymmetry for either of the phase diagrams reported in this work (Figures 4 and 5 of the main text). In the case of $\epsilon_{BC} = 1.5$, we were unable to converge an initial field for α-Al_2O_3. Finally, we were unable to obtain initial fields for either TiO_2 or CaF_2 for $\epsilon_{AB} = \epsilon_{BC} = 1.5$. In all cases, if we were unable to obtain an initial field at the desired conformational asymmetry, we assume the phase is highly unfavorable at the conditions being considered, and omit it from the analysis.

Table S1: Complete list of phases considered during generation of the phase diagrams. Table includes the name of the phase (Phase name); the label used to identify the phase in figures (Label Name); The crystal system and space group of the phase; the spatial discretization used in SCFT calculations for the phase (SCFT grid size); the number of nominally spherical particles in a unit cell of the phase (Particles per unit cell); the ratio of the number of particles composed of AB chains to the number of particles composed of B′C chains (AB:B′C particle ratio).

Phase name	**Label name**	**Crystal system**	**Space group**	**SCFT grid size**	**Particles per unit cell**	**AB:B′C particle ratio**
$MgZn_2$	C14	Hexagonal	$P6_3/mmc$	64x64x104	12	2:1
$MgCu_2$	C15	Cubic	$Fd\bar{3}m$	96x96x96	24	2:1
W	bcc	Cubic	$Im\bar{3}m$	48x48x48	2	0 or 1*
CsCl	alt-bcc	Cubic	$Pm\bar{3}m$	64x64x64	2	1:1
Cu	fcc	Cubic	$Fm\bar{3}m$	48x48x48	4	0 or 1*
Hexagonally packed cylinders	hex	Hexagonal	p6mm	48x48	N/A	0 or 1*
Alternating hex	alt-hex	Hexagonal	p6mm	48x48	N/A	2:1
Inverted alt-hex	$(\text{alt-hex})_i$	Hexagonal	p6mm	48x48	N/A	1:2
Nb_3Sn	A15	Cubic	$Pm\bar{3}n$	64x64x64	8	1:3
AlB_2	AlB_2	Hexagonal	P6/mmm	64x64x64	3	2:1
sapphire (α-BN)	α-Al_2O_3	Trigonal	$R\bar{3}c$	64x64x64	10	3:2
α-BN	α-BN	Hexagonal	$P6_3/mmc$	48x48x64	4	1:1
CaF_2	CaF_2	Cubic	$Fm\bar{3}m$	64x64x64	12	2:1
Li_3Bi	Li_3Bi	Cubic	$Fm\bar{3}m$	64x64x64	16	3:1
Inverted Li_3Bi	$(Li_3Bi)_i$	Cubic	$Fm\bar{3}m$	64x64x64	16	3:1
rocksalt	NaCl	Cubic	$Fm\bar{3}m$	64x64x64	8	1:1
ReO_3	ReO_3	Cubic	$Pm\bar{3}m$	64x64x64	4	3:1
σ-FeCr	σ	Tetragonal	$P4_2/mnm$	128x128x64	30	1:2**
TiO_2	TiO_2	Tetragonal	$P4_2/mnm$	64x64x42	6	1:2
ZnS	ZnS	Cubic	$F\bar{4}3m$	64x64x64	8	1:1

*These structures represent the AB-rich and B′C-rich morphologies considered for macrophase separation. All particles are composed of the majority species, with the minority located in interstitial sites.

**Particle assignment for σ is not trivial given the complexity of the structure. Here, B′C is placed in particles with volume above the number-averaged particle volume for the phase (Wyckoff positions 4f, 8i′, and 8j) while AB is placed in particles with volumes below this average (Wyckoff Positions 2b, and 8i), according to the volumes computed by Reddy et al. using the diblock foam model.[S21] This "above average" vs "below average" criteria was chosen for consistency with the Laves phases, in which B′C was assigned to the larger particles.

S5 Laves Phase Degeneracy

The main text reports that choice of Laves phase to use in the analysis would have little impact on the results because the Laves phases are found here to be nearly degenerate in free energy. To support this claim, Figure S3 shows the free energy of the C15 Laves phase relative to C14 based on the canonical ensemble SCFT calculations used to generate the phase diagram in Figure S4. We have chosen to use the C14 phase as the representative Laves phase in our analysis because our data show that it is, within the Laves phase field, more stable than C15. However, within this range, the total difference in the Laves phase free energies never exceeds 1×10^{-4} k_BT per chain of length N_{AB}. It is interesting to note that, over a brief composition window at lower ϕ_{AB} than the Laves phase field, C15 is briefly more stable than C14; regardless, it still remains metastable relative to macrophase separation.

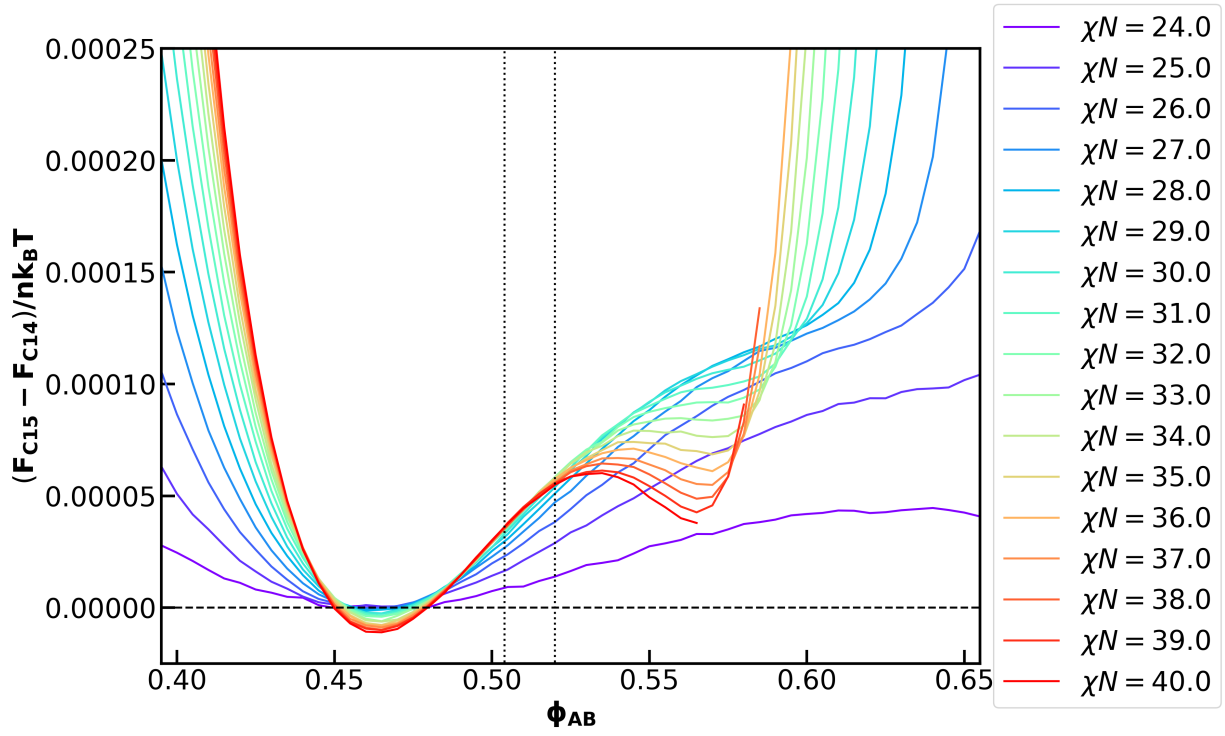

Figure S3: The energy of the C15 Laves phase relative to that of C14 from canonical ensemble SCFT data used to generate the phase diagram in Fig. 4 of the main text and Figure S4 here. The vertical dotted lines represent the bounds (in ϕ_{AB}) of Figure S4b and Fig. 4b, and serve as a guide for the range relevant to the Laves phase field reported in this work.

S6 Phase Diagram

In this work, most of the calculations have been done in the canonical ensemble, with the grand-canonical ensemble reserved for resolving 3-phase coexistence and the region near the ODT. In the canonical ensemble, system composition is specified directly via blend fractions, which are bound on [0,1]. This naturally-bounded domain allows energy profiles (sweeps in blend fraction with other parameters fixed, such that common tangent calculations can be completed) to be computed in parallel at a variety of conditions without concern that the resultant data will miss the coexistence region. In contrast, the chemical potential in the grand-canonical ensemble is specified rather than the blend fraction. The chemical potential is not similarly bounded, and the numerical range in which coexistence would be observed is not known a priori. It is also not known how far the chemical potential at coexistence may shift with changes in, for example, segregation strength or chain length. By running canonical ensemble calculations in parallel at the desired parameter ranges (in our case, segregation strength) we can quickly obtain results over the desired range. When additional accuracy is needed, these initial results can then act as a guide to estimate chemical potential values when refining three-phase coexistence or the regions near disorder.

Construction of the phase diagram reported in Figure 4 for an alloy with $N_{\mathrm{B'C}}/N_{\mathrm{AB}} = 1.0$ and $\epsilon_{\mathrm{BC}} = 1.5$ started with initial sets of canonical ensemble SCFT calculations followed by common tangent constructions at $\chi N = 23.5$ (the lowest value at which the Laves phases converged) and integer values of χN from 24.0 to 40.0 to obtain a coarse map of the phase boundaries. Subsequent canonical ensemble, common-tangent calculations were then performed at increments of 0.5 in χN around the AB-rich and B′C-rich coexistence transitions points (such as where the AB-rich phase in coexistence with the Laves phase field changes from fcc to bcc, or from bcc to hex). These first two rounds of calculation considered only the Laves phases and the macrophase separation competitors. A third round of canonical ensemble calculations added the remaining competitors at a selection of segregation strengths. Below the transition to Laves-hex$_{\mathrm{AB}}$ coexistence, competing phases were run at all sampled

segregation strengths. Above this transition, we noticed that the AB-rich hex phase quickly out-competes the Laves phases and suspected that it would similarly outcompete the other sphere-forming morphologies. We chose to run the remaining competitors only at $\chi N = 30$, $\chi N = 40$, and at odd values of χN from 31 to 39 finding that, indeed, all competitors are similarly outcompeted by AB-rich hex with increasing χN. On the basis of this result, we chose not to run the competing phases at the remaining χN values. Finally, grand canonical ensemble calculations were used to refine the position of invariant points and map the region near the ODT.

Here, Figure S4 reports the same phase diagram as Fig. 4 of the main text, but includes the particular points used to generate the diagram. Each dot in Figure S4 represents a point at which we have collected SCFT data. Data were collected at the highest density near invariant points where grand canonical ensemble was used to resolve the three-phase coexistence conditions. The reported data show that the splines used to draw the phase boundaries introduce no anomalous shapes and broadly reflect the collected data.

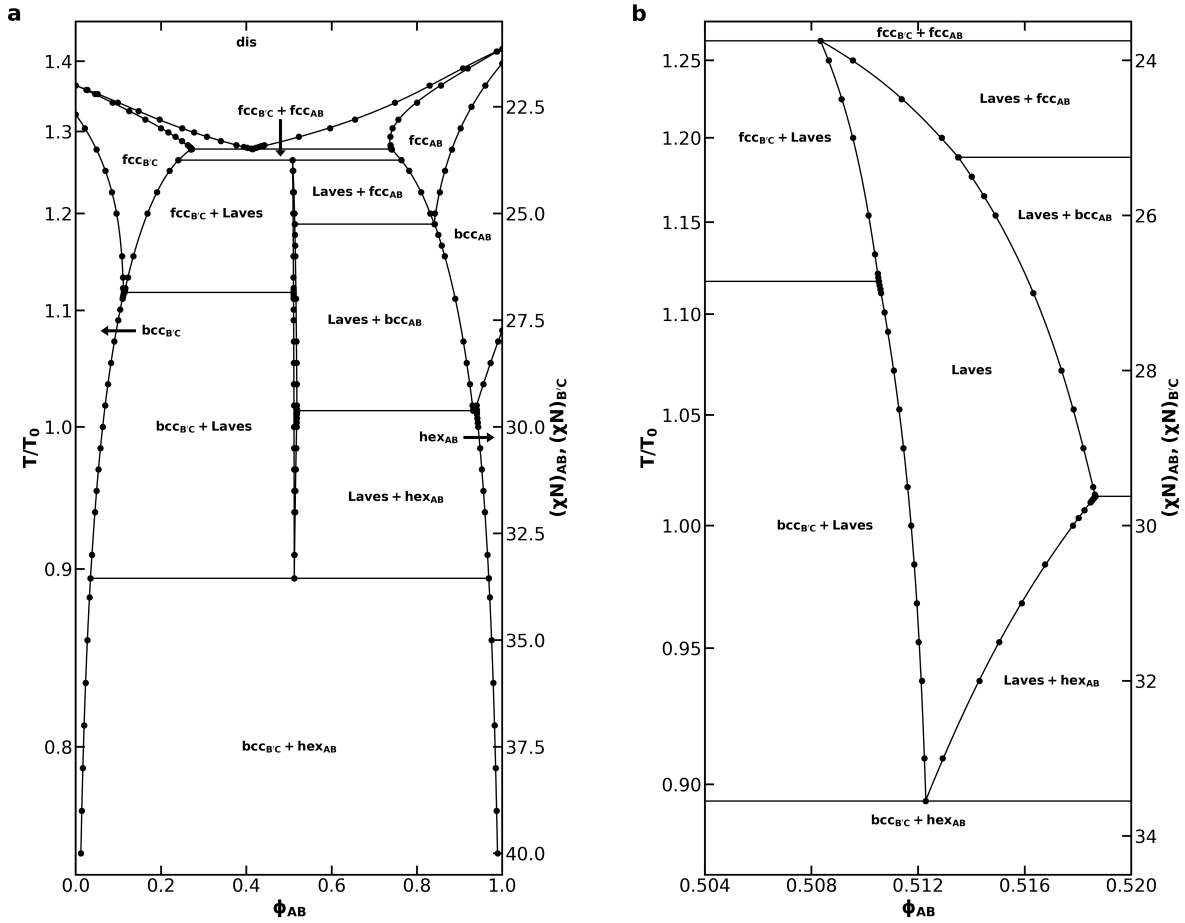

Figure S4: (a) Phase diagram for an AB/B′C alloy with $N_{\mathrm{B'C}}/N_{\mathrm{AB}} = 1.0$, $f_{\mathrm{A}} = f_{\mathrm{C}} = 0.20$, $\epsilon_{\mathrm{AB}} = 1.0$, $\epsilon_{\mathrm{BC}} = 1.5$, and assuming purely enthalpic χ values such that $\chi_{\mathrm{AC}} N_{\mathrm{AB}} = 2\,(\chi N)$ at all T and (b) a detailed view of the Laves phase field within that phase diagram. Points indicate conditions at which we collected SCFT data. The reference temperature, T_0, was chosen to correspond to $\chi N = 30$. Non-linear segments of the phase diagram are drawn using cubic splines fit to the sampled data.

References

(S1) `https://github.com/dmorse/pscfpp`, (accessed May 2022).

(S2) Arora, A.; Qin, J.; Morse, D. C.; Delaney, K. T.; Fredrickson, G. H.; Bates, F. S.; Dorfman, K. D. *Macromolecules* **2016**, *49*, 4675–4690.

(S3) `https://pscf.readthedocs.io/en/latest/index.html`, (accessed September 2022).

(S4) Matsen, M. W. *J. Phys. Condens. Mat.* **2002**, *14*, R21–R47.

(S5) Fredrickson, G. H. *The Equilibrium Theory of Inhomogeneous Polymers*; Oxford University Press: Oxford, United Kingdom, 2006.

(S6) Shi, A. In *Variational Methods in Molecular Modeling*; Wu, J., Ed.; Molecular Modeling and Simulation; Springer Singapore: Singapore, 2017; pp 155–180.

(S7) Sinturel, C.; Bates, F. S.; Hillmyer, M. A. *ACS Macro Lett.* **2015**, *4*, 1044–1050.

(S8) Matsen, M. W. *Eur. Phys. J. E* **2009**, *30*, 361.

(S9) Thompson, R. B.; Rasmussen, K. O.; Lookman, T. *J. Chem. Phys.* **2004**, *120*, 31–34.

(S10) Arora, A.; Morse, D. C.; Bates, F. S.; Dorfman, K. D. *J. Chem. Phys.* **2017**, *146*.

(S11) Tyler, C. A.; Morse, D. C. *Macromolecules* **2003**, *36*, 8184–8188.

(S12) McQuarrie, D. A. *Statistical thermodynamics*; Harper & Row, 1973.

(S13) Whitmore, M. D.; Noolandi, J. *Macromolecules* **1985**, *18*, 2486–2497.

(S14) `https://docs.scipy.org/doc/scipy/reference/generated/scipy.interpolate.UnivariateSpline.html`, (accessed September 2022).

(S15) `https://docs.scipy.org/doc/scipy/reference/generated/scipy.optimize.root.html`, (accessed September 2022).

(S16) More, J. J.; Garbow, B. S.; Hillstrom, K. E. *User guide for MINPACK-1*; Report ANL-80-70, 1980.

(S17) Matsen, M. W. *Phys. Rev. Lett.* **1995**, *74*, 4225–4228.

(S18) Magruder, B. R.; Park, S. J.; Collanton, R. P.; Bates, F. S.; Dorfman, K. D. *Macromolecules* **2022**, *55*, 2991–2998.

(S19) Xie, N.; Liu, M.; Deng, H.; Li, W.; Qiu, F.; Shi, A.-C. *J. Am. Chem. Soc.* **2014**, *136*, 2974–2977.

(S20) Xie, J.; Li, Y.; Shi, A. *Macromol. Theory Simul.* **2021**, *2100053*, 2100053.

(S21) Reddy, A.; Buckley, M. B.; Arora, A.; Bates, F. S.; Dorfman, K. D.; Grason, G. M. *Proc. Natl. Acad. Sci. USA* **2018**, *115*, 10233–10238.